Energy-based control of a dielectric elastomer cardiac assist device ⋆

Amal Hammoud * **Ning Liu** * **Yann Le Gorrec** *
Yoan Civet **,*** **Yves Perriard** **,***

* *Université Marie et Louis Pasteur, SUPMICROTECH, CNRS, institut FEMTO-ST, F-25000 Besançon, France*
** *Ecole polytechnique fédérale de Lausanne (EPFL), Integrated Actuators Laboratory (LAI), Neuchâtel, Switzerland*
*** *Ecole polytechnique fédérale de Lausanne (EPFL), Center for Artificial Muscles (CAM), Neuchâtel, Switzerland*

Abstract: This paper is concerned by the port-Hamiltonian modeling and control of a dielectric elastomer actuator designed for use in a cardiac assist device. The proposed nonlinear model captures the actuator's hyperelastic material behavior, viscoelastic damping, and electromechanical coupling, and remains valid for large deformations up to 40 %. An original Interconnection and Damping Assignment Passivity-Based Control strategy is developed to achieve closed-loop stabilization at a desired position. The accuracy of the multiphysics model and the performances of the proposed controller are experimentally validated.

Keywords: Mechatronic system estimation, identification, control; Dielectric elastomer actuators; Model identification; Port-Hamiltonian systems; Passivity-based control

1. INTRODUCTION

The technology of cardiac assist devices has been widely developed for almost six decades. Most solutions propose to replace or assist the heart with a ventricle simulator (Davies et al., 2024) or a rotary pump (Sen et al., 2016), etc. However, these solutions, while attractive, are often not fully bio-compatible, lack non-invasiveness, or too bulky with complex mechanism. Recent progresses in the field of soft actuators has led to the development of soft implantable cardiac assist devices. In (Almanza et al., 2021), researchers have studied a dielectric elastomer actuator (DEA) tube, which can replace part of the aorta, and help reduce the heart load with synchronized electric stimulus, as illustrated in Fig. 1a.

Different from conventional actuators, DEAs possess advantages of fast response time, light weight, low energy consumption, compliant structure, and good biocompatibility, making them promising candidates for biomedical devices. DEAs are composed of hyperelastic elastomer, sandwiched between flexible electrodes. The application of voltage can cause a significant deformation of the actuator. Despite the aforementioned advantages, a major drawback of DEAs is their electro-mechanical instability. As explained in (Zhao et al., 2007), this instability comes from the interaction between the applied electric field and the resulting mechanical deformation. When a certain voltage (kilovolts) is applied to the actuator, the electric field induces a Maxwell stress that compresses the DEA in the direction of its thickness, and thereby increases the electric field, causing further thinning of the actuator until it collapses. From a dynamic modeling and control point of view, this instability due to the aforementioned positive feedback can be compensated by an appropriate closed-loop control strategy.

In this article, we focus on the synthesis of control laws from physical models. Therefore, a dynamic model that describes the DEA properties, including **large deformations**, **hyperelastic behavior**, **creep phenomenon**, and **electro-mechanical coupling**, is necessary. Among all possible models, and with some reasonable assumptions, lumped parameter models are easier to derive and use for both numerical simulation and control design. Several physics-based models have been studied in the literature. In (Sarban and Jones, 2012), a nonlinear viscoelastic model is considered, with a feedforward term to control the vibration of the DEA. Both geometrical and hyperelastic material non-linearities are discussed in (Rizzello et al., 2015), with PID and H_∞ controllers for position control. In (Rizzello et al., 2016), this model was enhanced by incorporating viscoelastic elements and treated as a linear parameter-varying system, enabling the design of a robust position controller through linear matrix inequality. Other models similar to the one presented in Rizzello's work are listed in (Bernat et al., 2020; Liu et al., 2022; Zou et al., 2024; Hammoud et al., 2024). Among them, both (Liu et al., 2022) and (Hammoud et al., 2024) refer to the considered DEA tube cardiac assist device. The former focuses on modeling large deformations, hyperelasticity, viscoelastic behaviors, and electromechanical instability. The proposed model has been validated by experimental

⋆ This work has been funded by Germaine de Staël Funding Programme PHC N° 50645TH, and International Collegium SMYLE. This work has been achieved in the frame of the EIPHI Graduate school (contract "ANR-17-EURE-0002"). The fourth and fifth authors acknowledge the Werner Siemens Foundation.

measurements with more than 80.27% of accuracy. Besides, the DEA deformation strain reaches up to **48**%. The latter models the DEA within the port-Hamiltonian system (PHS) framework, and proposes a control by interconnection (CBI) methodology with integral action to both stabilize the DEA at desired positions, and to reject external disturbances. But the material behavior considered in (Hammoud et al., 2024) remains linear with linear constitutive relations. In the considered scenarios, the deformation strain is less than **10**%, which is only valid for small deformations.

The models mentioned above describe only the mechanical dynamics of DEAs. Their electrical behavior is treated as quasi-static, with the resulting electrostatic force derived from a nonlinear mapping of the applied voltage. The multiphysics modeling of DEAs has been studied in both (Kaaya et al., 2022) and in (Rizzello et al., 2017). The voltage is added as a new state variable in (Kaaya et al., 2022). However, the electromechanical coupling is treated in a one-way manner, considering only the effect of voltage on the mechanical momentum balance, while the influence of mechanical deformation on the electric current is disregarded. This is due to the choice of voltage as a state variable that is not naturally treated from the energy point of view. The proposed model is then linearized, such that PID and H_∞ controllers can be designed from the linearized system. On the other hand, the work in (Rizzello et al., 2017) models the multiphysics dynamics of a DEA membrane within the PHS framework. Different from the voltage, the state variable for the electrical subsystem is the electric charge, which comes naturally from the electric energy function. The dual electro-mechanical coupling appears in both the generated electrostatic force and the change of the capacitance with the mechanical deformation.

PHSs were initially introduced in 1992 in (Maschke et al., 1992). They are based on the use of energy and co-energy variables, Dirac structure and dissipation elements, which allow them to describe energy exchanges among different multiphysical subsystems, as well as with their environment (Duindam et al., 2009).

In addition to their use for modeling DEAs in (Rizzello et al., 2017; Hammoud et al., 2024), PHSs have proven to be effective in modeling other types of soft actuators, such as piezoelectric actuators in (Macchelli et al., 2004), ionic polymer metal composites actuators in (Liu et al., 2021), and hydraulically amplified self-healing electrostatic actuators in (Cisneros et al., 2025). Regarding controller design, the Hamiltonian (*i.e.*, the stored energy) is a good Lyapunov candidate function. If the open-loop PHS is connected with a controller within a PHS form in an energy-preserving way, the closed-loop system is again a PHS (van der Schaft, 2017). Moreover, PHS are inherently passive, which allows for the use of passivity-based control approaches, such as the aforementioned CBI, and Interconnection and Damping Assignment Passivity-based Control (IDA-PBC) (Ortega et al., 2001).

This paper is an extension of (Liu et al., 2022) and (Hammoud et al., 2024), with the following contributions:

(1) Following ideas from (Liu et al., 2022), the hyperelastic and viscoelastic properties of the material are considered and formulated in the port-Hamiltonian (PH) framework, to cope with a larger range of deformation.
(2) The electrical dynamics is investigated in the model with a simplified RC circuit, similar to what is done in (Rizzello et al., 2017). However, we consider a multilayered DEA with more complex geometry. Moreover, the electro-mechanical coupling lies in both the co-energy variables and in the dissipation matrix, which is not the case in (Rizzello et al., 2017).
(3) The proposed model is validated experimentally with different campaigns of measurements.
(4) Lastly, based on the multiphysics model, we propose a new IDA-PBC controller to stabilize the actuator at a desired position. This controller is later validated experimentally.

The rest of this paper is organized as follows: Section 2 describes the PHS modeling of the DEA cardiac assist device. Section 3 presents some results on the model's parameter estimation from experimental measurements. Section 4 proposes a new IDA-PBC control strategy to stabilize the DEA tube at a desired position. The experimental validation of the controller is given in Section 5. Finally, Section 6 provides some conclusions and perspectives.

2. DYNAMIC MODELING OF THE DEA TUBE

The schematic representation of the DEA integrated in the cardiovascular system is illustrated in Fig. 1a, with the DEA tube under investigation shown in Fig. 1b. The middle point of the tube has a radius of $R(t)$ and a thickness of $h(t)$. The DEA is made from Elastosil silicone films and carbon-based electrodes. They are stacked layer by layer (cf. Fig. 2a), and then rolled twice to make a tube, as presented in Fig. 2b. The initial thickness of each active layer is denoted by h_{a0}. We refer readers to (Almanza et al., 2021) for a detailed description of the fabrication.

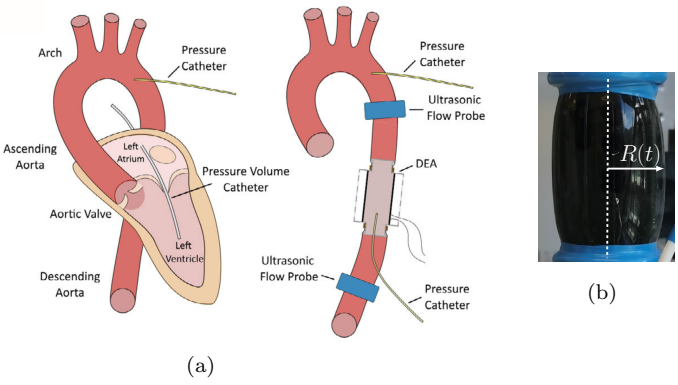

Fig. 1. (a) Schematic representation illustrating the integration of the DEA in the left part of the heart (Martinez et al., 2023). (b)Multilayered DEA tube.

2.1 Mechanical subsystem modeling

We assume that the deformation of the DEA tube is axisymmetric. Furthermore, the tube has its largest radial

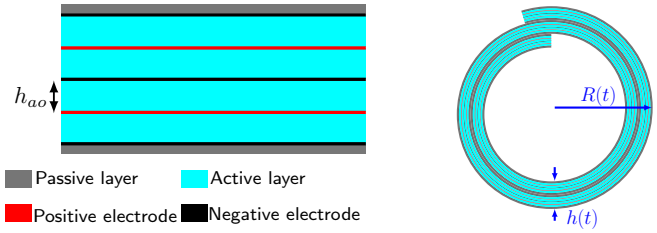

(a) (b)

Fig. 2. (a) Sectional view of DEA before rolling. (b) Sectional view of DEA after two rolls (Liu et al., 2022).

deformation around the middle point. Under the assumption that the material is incompressible, the thickness reaches its minimum at this point. Consequently, this point encounters an important electric field, which implies that the DEA tends to experience electro-mechanical instability near the middle point of the tube. Moreover, since the torsion is relatively small, the DEA is assumed to have only elongation and flexion. Therefore, the mechanical deformation of the DEA tube is simplified by a nonlinear mass-spring-damper model depicted in Fig.3a.

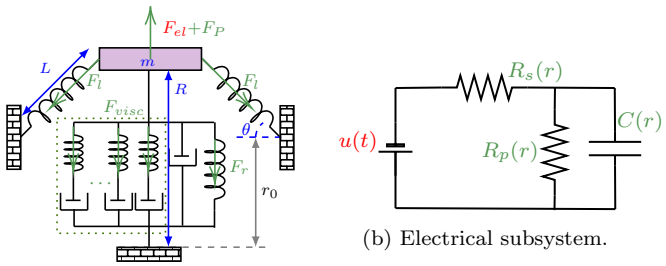

(a) Mechanical subsystem.

(b) Electrical subsystem.

Fig. 3. Schematic representation of the DEA model.

Given $r(t)$, the radial deformation, the geometric relations describing the tube deformation and elastomer expansion are $R(t) = r(t) + r_0$, and $L(t) = \sqrt{r(t)^2 + l_0^2}$, with r_0 and l_0 the initial radius and length, respectively. Moreover, the deformation angle is derived by: $\sin\theta(t) = r(t)/L(t)$.

The two opposite springs in Fig. 3a represent the longitudinal elastic forces F_l of the DEA tube, and are assumed linear with constant stiffness K_1, whereas the vertical spring models the hyperelastic deformation force F_r that is nonlinear. The damper in parallel to F_r is linear with a damping coefficient η_0. Moreover, several spring-damper elements have been added in parallel with constant stiffness coefficient k_j and damping coefficient d_j for the jth element (with $j \in [1, n]$, and n referring to the total number of spring-damper elements arranged in parallel). These visco-damping components are associated with the creep phenomenon (Liu et al., 2022), which corresponds to a time-dependent gradual deformation under constant loading. The value of n requires further comparison between simulation results and experimental measurements. The DEA tube is pre-stretched by a pressure force $F_P = S(r)P(t)$, where $P(t)$ is the applied pressure, and $S(r) = 4\pi\left(R(r) + r_0\right)L(r)$ denotes the inner surface area. The actuator is driven by an electrostatic force F_{el}, which will be described in detail later.

The stored energy (Hamiltonian) of this subsystem is:

$$H_m(r, d_j, p) = H_{mr}(r) + \frac{1}{2}\sum_{j=1}^{n} k_j d_j^2 + \frac{1}{2}\frac{p^2}{m}, \tag{1}$$

with:

$$H_{mr}(r) = K_1 l(r)^2 + V_{ol} W(r),$$

where V_{ol} is the DEA volume and is considered constant, $d_j(t)$ denotes the jth spring deformation in the visco-damping part, $p(t)$ represents the DEA momentum, and $W(r)$ stands for the strain energy density of the hyperelastic spring. Different models of the strain energy density have been proposed in the literature. Following previous works in (Martinez et al., 2021; Liu et al., 2022), we adopt the following Yeoh's model:

$$W(r) = C_1\mathcal{I}(r) + C_2\mathcal{I}(r)^2 + C_3\mathcal{I}(r)^3, \tag{2}$$

where $C_1 > 0$, $C_2 < 0$, $C_3 > 0$ are constant material parameters. The negative C_2 is responsible for the material softening (Yeoh, 1993). $\mathcal{I} = I_1 - 3$ with $I_1(r)$ denoting the first invariant of the left Cauchy-Green deformation tensor:

$$I_1(r) = \lambda_1^2 + \lambda_2^2 + \lambda_3^2, \tag{3}$$

where $\lambda_1(r) = L(r)/l_0$, $\lambda_2(r) = R(r)/r_0$, and λ_3 are stretches along longitudinal, radial, and thickness directions, respectively. Under the material incompressibility assumption, one gets:

$$\lambda_3(r) = 1/\left(\lambda_1(r)\lambda_2(r)\right). \tag{4}$$

Remark 1. Substituting Eq.(4) to (3), we get the following inequality:

$$I_1 = \lambda_1^2 + \lambda_1^2 + \frac{1}{\lambda_1^2\lambda_2^2} \geq 3\sqrt[3]{\lambda_1^2\lambda_1^2\frac{1}{\lambda_1^2\lambda_2^2}} = 3.$$

However, due to the negativity of C_2 in Eq.(2), we cannot guarantee that the strain energy density $W(r)$ is always positive. To make sure that $W(r) > 0$ within the deformation range, we will consider this as an inequality constraint in Section 3.1 dealing with parameters estimation.

Remark 2. One could also consider the longitudinal spring F_l nonlinear, *i.e.*, as in (Liu et al., 2022). Nevertheless, this adjustment appears unnecessary, as the simulation results obtained from our model closely match the experimental data when the DEA undergoes large deformations.

From Eq.(1), we choose r, p and d_j as energy variables, and the corresponding co-energy variables are derived as:

$$\nabla_r H_m = 2K_1 l\sin\theta + V_{ol}\frac{\partial W}{\partial r}, \tag{5}$$

$$\nabla_p H_m = \frac{p}{m}, \tag{6}$$

$$\nabla_{d_j} H_m = k_j d_j, \tag{7}$$

where the first term of Eq.(5) represents the spring forces F_l that are projected on the radial direction, the second term is related to the hyperelastic spring force F_r, the sum of $\nabla_{d_j} H_m$ for $j \in [1, n]$ refers to the visco-damping force F_{visc} as depicted in Fig. 3a. Therefore, the equation of motion of the simplified mass-spring-damper system is formulated as:

$$\dot{p} = -\nabla_r H_m - \eta_0\nabla_p H_m - \boldsymbol{\nabla}_d H_m + F_{el} + F_P, \tag{8}$$

$$\dot{d}_j = \nabla_p H_m - \frac{1}{\eta_j}\nabla_{d_j} H_m, \tag{9}$$

with $\boldsymbol{\nabla}_d H_m = \sum_{j=1}^{n} \nabla_{d_j} H_m$.

2.2 Electrical subsystem modeling

The electrostatic force F_{el} mentioned in Eq.(8) comes from the Maxwell stress, which is formulated as:

$$\sigma_{\text{maxwell}}(t) = -\epsilon_0 \epsilon_r E(t)^2, \tag{10}$$

where ϵ_0 and ϵ_r are the vacuum permittivity and relative permittivity, respectively. $E(t)$ denotes the electric field. We assume that the elastomer is ideal, which means that both ϵ_0 and ϵ_r are constant.

The electrical subsystem is modeled as an electric circuit that is presented in Fig. 3b. The dielectric elastomer can be considered as a capacitance $C(r)$. The resistance in series $R_s(r)$ represents the electrode's resistance, while $R_p(r)$ in parallel refers to the current leakage. The coupling between the mechanical and electrical subsystems is contained in the expressions of $C(r)$, $R_s(r)$ and $R_p(r)$, which are:

$$C(r) = 4\pi N_c \epsilon_0 \epsilon_r \frac{R(r)L(r)}{h_a(r)}, \tag{11}$$

$$R_s(r) = \frac{N_c \rho_d}{2\pi} \frac{L(r)}{R(r) h_e(r)}, \tag{12}$$

$$R_p(r) = \frac{N_c \rho_l}{4\pi} \frac{h_a(r)}{R(r)L(r)}, \tag{13}$$

where N_c represents the number of active layers, $h_a(r)$ is the thickness of one active layer, $h_e(r)$ gives the thickness of the electrodes, ρ_d and ρ_l denote the resistivity of the dielectric and of the leakage, respectively.

The Hamiltonian of the electrical subsystem writes:

$$H_e(r, Q) = \frac{1}{2} \frac{Q^2}{C(r)}, \tag{14}$$

where Q is the electric charge that follows the equation:

$$\dot{Q}(t) = -\frac{1}{R_e(r)} \nabla_Q H_e + \frac{1}{R_s(r)} u(t). \tag{15}$$

with $R_e(r) = R_s(r) R_p(r) / \left(R_s(r) + R_p(r)\right)$.

2.3 Overall system

The Hamiltonian of the full system is given by:

$$H(r, d_j, p, Q) = H_m(r, d_j, p) + H_e(r, Q). \tag{16}$$

As mentioned in Eq.(11)-(13), the radial deformation r modifies the electric components. In return, the electrical subsystem generates a force expressed as:

$$\nabla_r H_e = -\frac{1}{2} \frac{Q(t)^2}{C(r)^2} \nabla_r C. \tag{17}$$

Assumption 3. We assume that the multilayers of the DEA are closely attached during the deformation, and follow the same deformation stretch, *i.e.*,

$$\lambda_3(t) = h_a(t)/h_{a0} = h(t)/h_0. \tag{18}$$

Substituting Eq.(4) and (18) into (11), one can calculate:

$$\nabla_r C = \frac{8\pi N_c \epsilon_0 \epsilon_r}{l_0 r_0 h_{a0}} \left[R(r)L(r)^2 + R(r)^2 L(r) \sin\theta(r)\right]. \tag{19}$$

Remark 4. If one assumes that the electrical part is quasi-static without dissipation, *i.e.*, $u = Q/C$, and applies Eq. (18) and (19), then Eq.(17) is equivalent to the electrostatic force F_{el} calculated from the Maxwell stress:

$$\nabla_r H_e = N_c \left(S_r(r) + S_l(r) \sin\theta(r)\right) \sigma_{\text{maxwell}}(t) = F_{el},$$

where $S_r(r) = 4\pi L(r) h_a(r)$ represents the section area along the circumferential direction that is projected on the radial direction, and $S_l = 4\pi R(r) h_a(r)$ refers to the cross-section area in the longitudinal direction of each active layer. One could find a detailed illustration of $S_r(r)$ and $S_l(r)$ in (Liu et al., 2022).

Therefore, Eq.(8), (9) and (15) can be reformulated by the following input-state-output PHS:

$$\dot{x} = (J - R(x)) \nabla_x H + g_P(x) P(t) + g_u(x) u(t), \tag{20a}$$

$$y_P = g_p^T(x) \nabla_x H, \tag{20b}$$

$$y_u = g_u^T(x) \nabla_x H, \tag{20c}$$

with $x = [r,\ p,\ d_j,\ Q]^T$, and

$$J = \begin{pmatrix} 0 & 1 & \mathbf{0} & 0 \\ -1 & 0 & -\mathbf{1} & 0 \\ \mathbf{0}^T & \mathbf{1}^T & 0 & \mathbf{0}^T \\ 0 & 0 & \mathbf{0} & 0 \end{pmatrix}, \quad R(x) = \begin{pmatrix} 0 & 0 & \mathbf{0} & 0 \\ 0 & \eta_0 & \mathbf{0} & 0 \\ \mathbf{0}^T & \mathbf{0}^T & \mathcal{R}_\eta & \mathbf{0}^T \\ 0 & 0 & \mathbf{0} & \frac{1}{R_e(r)} \end{pmatrix},$$

$$g_P(x) = [0\ S(r)\ \mathbf{0}\ 0]^T, \qquad g_u(x) = \left[0\ 0\ \mathbf{0}\ \tfrac{1}{R_s(r)}\right]^T,$$

where $\mathbf{0} \in \mathbb{R}^{1\times n}$ and $\mathbf{1} \in \mathbb{R}^{1\times n}$ are vectors of 0 and 1, respectively. $0 \in \mathbb{R}^{n\times n}$ is a matrix of 0. $\mathcal{R}_\eta \in \mathbb{R}^{n\times n}$ stands for a diagonal matrix of $\frac{1}{\eta_j}$. The couplings between mechanical and electrical subsystems lie in both the electrostatic force derived from Eq.(17) and the deformation-dependent RC elements in Eq.(11)-(13).

3. SYSTEM IDENTIFICATION

Several physical parameters in Eq. (20) are not measurable, and need to be identified from experimental data. The experimental setup is depicted in Fig. 4.

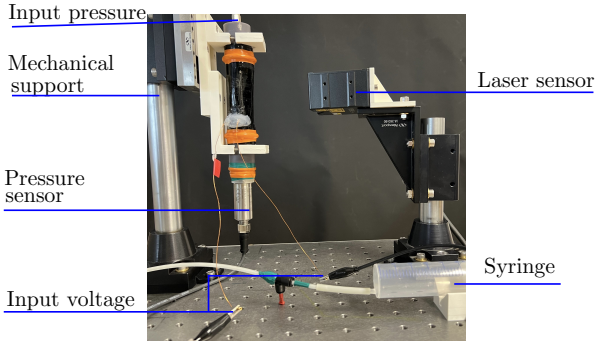

Fig. 4. Measurement setup for the DEA tube.

The DEA tube is clamped at both sides and pre-stretched by applying pressure through a syringe. Input voltage is generated through a computer equipped with a dSPACE board, and then amplified with a high voltage amplifier Trek 609-B3 with a gain of 1000. This amplifier also helps to measure the output current. The pressure sensor Baumer PBMN-25 and laser position sensor Keyence LJ-V7080 are dedicated to the measure of the pressure inside the tube chamber, and to the measure of the radial profile deformation, respectively. These measurements are sampled and recorded with dSPACE and ControlDesk with a sampling rate of 1kHz. The dimensions and known parameters of the considered tube are the following: $l_0 =$

2.35cm, $r_0 = 1.45$cm, $h_0 = 1$mm, $h_{a0} = 100\mu$m, $h_{e0} = 8\mu$m, $m = 14.68$g, and $\epsilon_0 = 8.854$nF/m. Unknown parameters are K_1, C_1, C_2, C_3, k_j, η_0, η_j, ϵ_r, ρ_d, ρ_l.

3.1 Parameters estimation

The parameter estimation is an optimization problem that aims to minimize the distance (*i.e.*, sum squared errors) between the experimental measurements (**radius** and **current**) and the simulation ones. We employed the nonlinear least squares method with the Levenberg-Marquardt algorithm using Simulink's Parameter Estimator. This part of work is divided into three main steps. First, we focus only on the identification of $\Theta_1 = [K_1\ , C_1\ , C_2,\ C_3]^T$ with applied pressure as depicted in Fig. 5a, which increases slowly to make sure that the system is almost quasi-static. Moreover, according to *Remark* 1, we re-parameterize C_1, C_2 and C_3 with the following equations: $C_1 = C_\beta^2 + C_\gamma$, $C_2 = -2C_\alpha C_\beta$, $C_3 = C_\alpha^2$, with C_α, C_β and C_γ positive, such that the constraints for C_1, C_2 and C_3 are satisfied, and Eq.(2) can be reformulated as:

$$W(r) = (I_1(r) - 3)\left[(C_\alpha\,(I_1 - 3) - C_\beta)^2 + C_\gamma\right], \quad (21)$$

which is always positive along the deformation r.

The comparison between experimental measurements and simulation results is given in Fig. 5b, with identified parameters listed in Table 1.

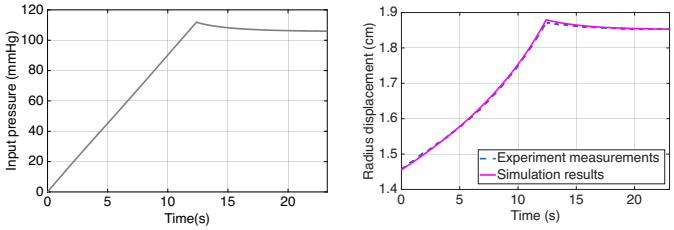

(a) Input pressure. (b) Comparison of radius.

Fig. 5. Identification of parameters in Θ_1.

Subsequently, the syringe is blocked at a fixed position. A 'step' input voltage is generated and sent to the DEA tube. It is worth mentioning that the rise time of the input voltage is limited to 20ms to avoid high current spikes and to prevent dielectric breakdown. The input pressure and voltage are measured and presented in Fig. 6a, which excite high frequency responses, and allow to identify the parameters in $\Theta_2 = [\eta_0, k_j, \eta_j, \epsilon_r]^T$. The number of viscoelastic elements is tested and goes up to $n = 4$. The identified parameters are illustrated in Table 1. Therefore, the comparison between experimental measurements and simulation results is presented in Fig.6b. One can observe a quick deformation of the DEA, followed by a slow deformation, which is the creep phenomenon that is introduced in Subsection 2.1.

Lastly, the two resistivity parameters ρ_d and ρ_l are estimated from the other current output measurement. The input pressure and voltage are the same as in Fig. 6a, with a focus on the time interval between $[0, 1]s$. The comparison results are shown in Fig. 7. We can see that the output current simulation follows a similar dynamic profile than in the experimental result. However, one could

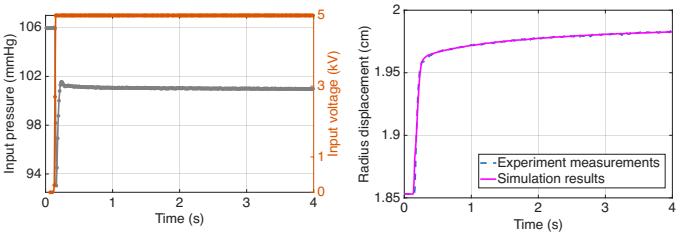

(a) Input pressure and voltage. (b) Comparison of radius.

Fig. 6. Identification of parameters in Θ_2.

still find a discrepancy during the decrease in the current. This may due to the fact that our electrical model is still simple with respect to the electronic fabrication of the DEA tube. In fact, there is a silver stick inside the DEA, which charges and discharges more quickly than the electrodes. Another possibility to improve the electrical subsystem is to consider more RC elements, as well as the winding, as discussed in (van Kessel et al., 2021).

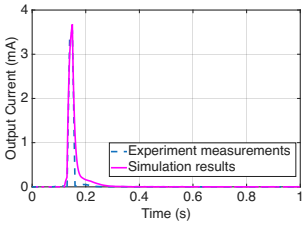

Fig. 7. Identification of ρ_d and ρ_l.

Table 1. Identified Parameters.

Parameters	Values	Parameters	Values
K_1	854.34 N/m	C_1	294.28 kPa
C_2	−26.09 kPa	C_3	0.76 kPa
η_0	59.20 Ns/m	k_1	1.14 kN/m
k_2	0.61 kN/m	k_3	0.55 kN/m
k_4	1.76 kN/m	η_1	4.84 kNs/m
η_2	0.13 kNs/m	η_3	2.40 kNs/m
η_4	1.18 Ns/m	ϵ_r	2.74
ρ_d	55.39 TΩ m	ρ_l	1.50 Ω m

The variations of elements in the electrical subsystem are depicted in Fig. 8. With inputs given in Fig. 6a, one can find a variation of the capacitance between $[17.3, 20.4]$nF. The resistance in series also increases along the radial deformation within an interval of $[495.5, 505.7]$kΩ, as illustrated with the blue solid curve in Fig. 8b. However, the resistance in parallel decreases in a scale of TΩ following the radial deformation, as presented in the green dashed curve.

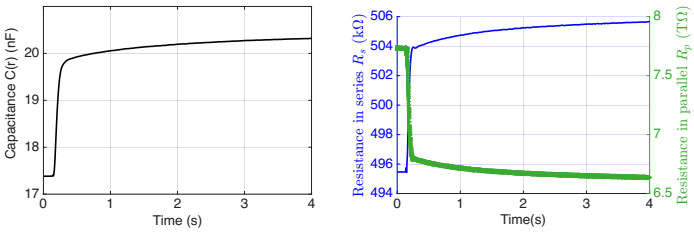

(a) Capacitance variation. (b) R_s and R_p variations.

Fig. 8. Simulation results of electric elements.

3.2 Model validation

The identified parameters are used to compare the simulation results with other different experimental results. One finds in Fig. 9a the validation of parameters Θ_1 and Θ_2 with radius measurements. The grey dashed lines represent the experimental radius measurements at the middle point of the tube. The solid lines represent simulation results obtained at various applied pressures and a voltage of 5kV. The orange and purple lines with circular markers correspond to simulation results at 4kV, under the same pressure conditions. The validation of ρ_d and ρ_l are realized with different applied voltages at 4kV and at 5kV, respectively. As shown in Fig. 9b, the simulation results closely match the experimental measurements of the output current. The validation errors for the output radius and current are shown in Fig. 9c and Fig. 9d, respectively.

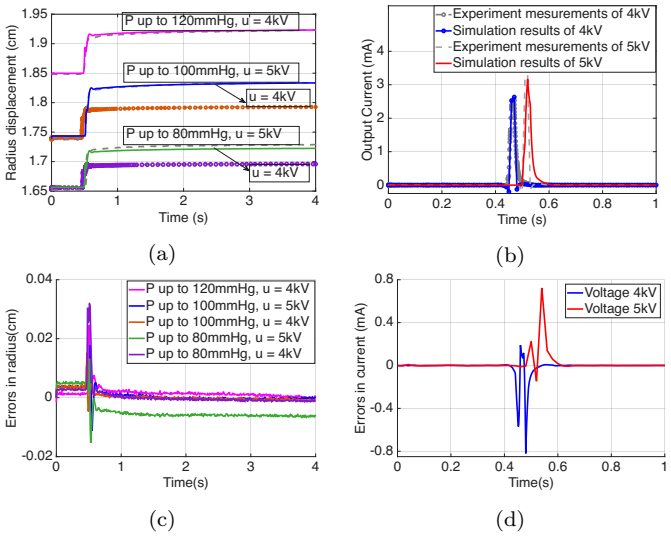

Fig. 9. Parameters validation.

To precisely evaluate the aforementioned model validation, root mean square error (RMSE) is provided in Table.2.

Table 2. RMSE of model validation in Fig. 9.

	Conditions	RMSE
Validation of Θ_1	$P = 120\,\text{mmHg},\ u = 4\,\text{kV}$	1.818×10^{-6}
	$P = 100\,\text{mmHg},\ u = 5\,\text{kV}$	1.736×10^{-6}
	$P = 100\,\text{mmHg},\ u = 4\,\text{kV}$	9.220×10^{-6}
and of Θ_2	$P = 80\,\text{mmHg},\ u = 5\,\text{kV}$	6.344×10^{-5}
	$P = 80\,\text{mmHg},\ u = 4\,\text{kV}$	1.252×10^{-6}
Validation of ρ_d	$u = 5\,\text{kV}$	1.412×10^{-7}
and ρ_l	$u = 4\,\text{kV}$	4.335×10^{-7}

To better assess the contributions of our model in comparison with existing alternative approaches, particularly those discussed in the Introduction, we have completed the Table 3.

4. PASSIVITY-BASED CONTROLLER DESIGN

The control objective is to stabilize the DEA tube at desired positions by using the input voltage in closed-loop.

[1] Electro-mechanical coupling that describes the energy exchange between electric and mechanical subsystems.

The model presented in Eq.(20) is intrinsically passive, and satisfies:

$$\frac{dH}{dt} = -\nabla_x^T H R(x) \nabla_x H + y_P P + y_u u \leq y_P P + y_u u.$$

The idea is to take advantage of this passivity property to design a passivity-based controller. One type of passivity-based control is the CBI that has already been proposed in (Hammoud et al., 2024). The open-loop PHS is connected to a PHS controller in a power-preserving way. The controller states are related to the plant system through structural invariants called Casimir functions. One can modify the closed-loop Hamiltonian (*i.e.,* **Energy shaping**) to change the system's equilibrium point and its dynamic properties, and modify the dissipation matrix by **damping injection**. The CBI was designed based on a simplified mechanical model of the system. However, this approach does not work on the electro-mechanical system due to the so called dissipation obstacle (Ortega et al., 2001). Therefore, another passivity-based control design method, IDA-PBC, is used in this paper, to overcome the dissipation obstacle, and to provide more degrees of freedom for the controller design.

During this part of the work, we concentrate only on the design of the controller with input voltage. In what follows, we present the methodology of IDA-PBC and the solution of the generated matching equations.

We start with a brief reminder on IDA-PBC control design. The aim is to design a state feedback to match the system with the desired closed-loop system:

$$\dot{x} = \left(J_d(x) - R_d(x)\right) \nabla_x H_d, \tag{22}$$

with $J_d(x) = -J_d^T$, $0 \leq R_d(x) = R_d(x)^T$, and H_d representing the desired closed-loop Hamiltonian. Putting Eq.(20) and (22) together, one obtains the following relation:

$$\left(J_d(x) - R_d(x)\right) \nabla_x H_d = \left(J - R(x)\right) \nabla_x H + g_u(x) u(t). \tag{23}$$

One can modify $J_d(x)$ to play with interconnections between subsystems, R_d to add more dissipation in closed-loop, or H_d to change the equilibrium/performances. The main challenge of the control design is to solve the matching equation (23). The classical approach consists in choosing J_d and R_d, and then computing H_d by solving the partial differential equations (PDEs) in Eq. (23). A direct solution of these PDEs is presented in (Ortega et al., 2001). However, the computation can quickly become complicated when non-linearities are introduced into the plant. Alternative approaches include replacing the resulting PDEs with algebraic inequalities (Acosta and Astolfi, 2009), transforming the PDEs into Pfaffian differential equations (Harandi and Taghirad, 2022), or reformulating the controller using a different storage function to avoid solving the PDEs altogether (Borja et al., 2016). Nevertheless, these methods are limited to specific systems that satisfy certain assumptions. Apart from solving the PDEs directly, (Rodríguez and Ortega, 2003) proposes to assign firstly H_d, and to determine subsequently J_d and R_d. However, the selection of the controller parameters in this method is constrained by an inequality condition. Moreover, the resulting control law exhibits a singularity when the desired equilibrium is located at the origin. Similar idea has been proposed in (Javanmardi et al., 2025) without the aforementioned application constraints.

Table 3. Comparison of existing control-oriented dynamic models for DEAs.

Models	Motion	Deformation strain	Hyperelasticity	Creep	E-M coupling [1]	Experiment validation
(Sarban and Jones, 2012)	Tube elongation	Less than 5%	–	√	–	√
(Rizzello et al., 2015)	Annular membrane out-of-plane deformation	30%	√	√	–	√
(Rizzello et al., 2016)		170%	√	√	–	√
(Rizzello et al., 2017)		–	√	√	√	–
Bernat et al. (2020)	Circular membrane out-of-plane deformation	–	√	√	–	√
(Kaaya et al., 2022)	Tube elongation	11.27%	√	–	√	√
(Zou et al., 2024)	Planar DEA, conical DEA, DEA with a minimum energy structure, and DEA with 2 degrees of freedom	–	–	√	–	√
(Liu et al., 2022)	Tube radial deformation	48%	√	√	–	√
(Hammoud et al., 2024)		Less than 10%	–	–	–	√
Current work		36.75%	√	√	√	√

In what follows, we present a novel design strategy that avoids solving the PDEs in the matching equation, and that overcomes the drawbacks in (Rodríguez and Ortega, 2003) and (Borja et al., 2016), which is applicable to a broader class of electro-mechanical systems.

Proposition 5. Choosing the interconnection and dissipation matrices as:

$$J_d = \begin{pmatrix} 0 & 1 & \mathbf{0} & 0 \\ -1 & 0 & -\mathbf{1} & \alpha \\ \mathbf{0}^T & \mathbf{1}^T & 0 & 0 \\ 0 & -\alpha & \mathbf{0} & 0 \end{pmatrix}, \quad R_d = \begin{pmatrix} 0 & 0 & \mathbf{0} & 0 \\ 0 & \eta_0 & \mathbf{0} & 0 \\ \mathbf{0}^T & \mathbf{0}^T & \mathcal{R}_\eta & \mathbf{0}^T \\ 0 & 0 & \mathbf{0} & \frac{1}{\delta} \end{pmatrix} \geq 0,$$

and Hamiltonian function

$$H_d = H_m + \frac{(Q-Q^*)^2}{2C_Q} + \frac{(Q^*)^2}{2C(r)} - H_{mr}(r^*) - \frac{(Q^*)^2}{2C(r^*)}, \quad (24)$$

with $C_Q > 0$, $\delta > 0$, and

$$Q^*(r^*) = \sqrt{\frac{2\left(C(r)\right)^2 \nabla_r H_m(r)}{\nabla_r C}}\Bigg|_{r=r^*}, \quad (25a)$$

$$\alpha(r,, r^*, Q) = \frac{\nabla_r C}{2\left(C(r)\right)^2} C_Q \left(Q + Q^*(r^*)\right), \quad (25b)$$

the control law:

$$u = R_s(r)\left[-\alpha\frac{p}{m} - \frac{(Q-Q^*)}{\delta C_Q} + \frac{1}{R_e(r)}\frac{Q}{C(r)}\right] \quad (26)$$

stabilizes asymptotically the closed-loop system Eq.(22) at equilibrium point $x^* = [r^*,\ 0,\ \mathbf{0}_{1\times 4}, Q^*]^T$.

Proof. Multiplying Eq. (23) with $g^\perp$, where $g^\perp = [I_{6\times 6},\ \mathbf{0}_{6\times 1}]$ is a full rank left annihilator of g_u, i.e $g^\perp g_u = \mathbf{0}_{6\times 1}$, one obtains:

$$g^\perp \left(J_d(x) - R_d(x)\right)\nabla_x H_d = g^\perp \left(J(x) - R(x)\right)\nabla H. \quad (27)$$

Consequently, we get the following matching equations:

$$\begin{aligned} &-\nabla_r H_d - \eta_0 \nabla_p H_d - \boldsymbol{\nabla}_d H_d + \alpha \nabla_Q H_d \\ &= -\nabla_r H - \eta_0 \nabla_p H - \boldsymbol{\nabla}_d H. \end{aligned} \quad (28)$$

By choosing $\nabla_p H_d = \nabla_p H$, $\boldsymbol{\nabla}_d H_d = \boldsymbol{\nabla}_d H$, and α as in (25b) and defining:

$$\nabla_Q H_d = \frac{Q - Q^*}{C_Q},$$

where Q^* is obtained from the open-loop system by setting $\dot{p} = 0$, the matching equation (28) can be simplified as follows:

$$\nabla_r H_d = \nabla_r H_m - \frac{\nabla_r C(r)}{2\left(C(r)\right)^2}\left(Q^*\right)^2.$$

Therefore, the closed-loop Hamiltonian is calculated as in Eq.(24) such that $H_d(r^*) = 0$. Substituting Eq.(25a) and (25b) into $\nabla_x H_d$, it follows that:

$$\nabla_x H_d(x^*) = 0. \quad (29)$$

Due to the strong nonlinearities in H_d, the second derivative $\nabla_r^2 H_d$ is calculated numerically to check that $\nabla_r^2 H_d(x^*) > 0$, which implies that the Hessian of H_d evaluated at x^* is positive definite. Consequently, the equilibrium x^* is a (locally) stable equilibrium.

Hence, we choose H_d as a Lyapunov function. Its time derivative writes:

$$\frac{dH_d}{dt} = -\eta_0 \left(\nabla_p H_d\right)^2 - \frac{1}{\eta_j}\left(\boldsymbol{\nabla}_d H_d\right)^2 - \frac{1}{\delta}\left(\nabla_Q H_d\right)^2 \leq 0.$$

It remains to show that the only solution associated with $dH_d/dt = 0$ is $p \equiv 0$, $d_j \equiv 0$, and $Q \equiv Q^*$, which implies $r \equiv r^*$. Using LaSalle's invariance principle, $x(t)$ converges to x^* asymptotically in closed-loop.

Finally, the control law u in Eq.(26) is calculated from:

$$u = g^\dagger \left(\left(J_d(x) - R_d(x)\right)\frac{\partial H_d}{\partial x} - \left(J(x) - R(x)\right)\frac{\partial H}{\partial x}\right),$$

with $g^\dagger = \left(g_u^T g_u\right)^{-1} g_u^T$.

The proposed control law adds a coupling between mechanical and electrical subsystems. The C_Q modifies the closed-loop capacitance, and δ introduces more damping.

With the identified model presented in Section 3, the DEA tube under investigation has an initial radius of 1.45cm, and is hereby pre-stretched with a radial deformation of 0.4cm. The control law defined in Eq. (26) is implemented to achieve a desired radius of 1.95cm with a rise time of 0.3s, as indicated by the grey dashed line in Fig.10a. Several values of C_Q are studied to evaluate the controller performance. Furthermore, increasing C_Q slows down the DEA deformation, but reduces the initial voltage peak, as highlighted in Fig. 10b. The influence of δ has also been investigated in Fig. 11. Increasing δ produces effects similar to those of C_Q, decelerating the system response while mitigating the initial voltage peak.

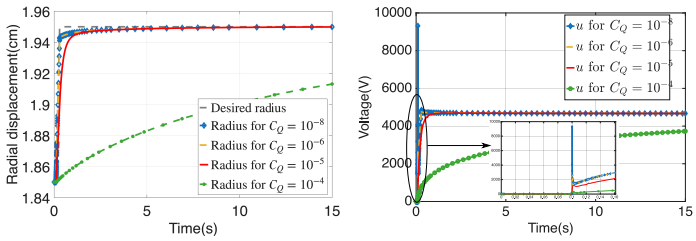

(a) Radius simulation. (b) Control input.

Fig. 10. IDA-PBC controller simulation with different C_Q.

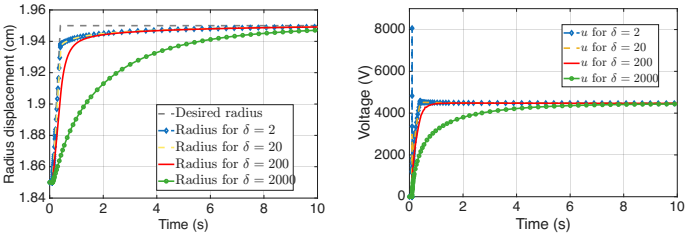

(a) Radius simulation. (b) Control input.

Fig. 11. IDA-PBC controller simulation with different δ.

Remark 6. As illustrated in Fig. 10 and Fig. 11, the IDA-PBC controller stabilizes the radius at the desired position but is unable to eliminate the creep phenomenon of the plant. This behavior is consistent with the matching equation Eq.(28), as the closed-loop Hamiltonian does not modify the mechanical energy component $\nabla_d H_d$.

The tuning of the parameters C_Q and δ hereby aims to minimize the following cost function:

$$f_{cost}(C_Q, \delta) = \int_0^{t_f} \frac{t|r(C_Q,\delta) - r^*|}{0.0001} dt + \int_0^{t_f} \frac{|\dot{u}(C_Q,\delta)|^2}{10^8} dt, \tag{30}$$

where the first term refers to the normalized integral of time-weighted absolute error (Martins, 2005), and the second one stands for the normalized oscillation of the control input. The optimization has been realized with Nelder-Mead simplex direct search. One can find the iteration values of the cost function in Fig.12, with a minimizer of

$$C_Q = 2.9973 \times 10^{-7}, \qquad \delta = 9.3064 \times 10^4,$$

which gives the closed-loop dynamic and control input as depicted by red curves with square markers in Fig. 13a and 13b, respectively. The DEA stabilizes at both desired position of 1.88cm and 1.95cm with fast rise time and smooth control input voltage.

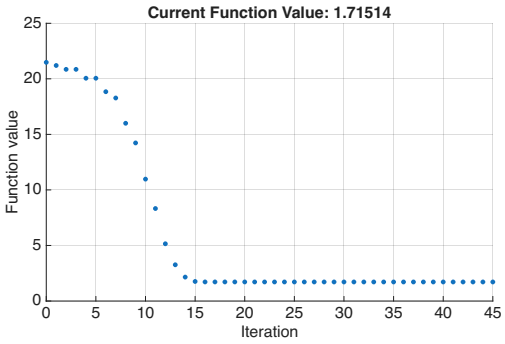

Fig. 12. Iterations of cost function (30).

Moreover, one can find the comparison between the optimized IDA-PBC controller, and a classical PID controller in Fig. 13. The PID controller is initially tuned in order to stabilize the DEA with similar performances at 1.88cm. However, once the desired position increases to 1.95cm, the closed-loop system becomes unstable, which illustrates that classical PID control can stabilize nonlinear systems only within a small neighborhood of the equilibrium, but loses stability beyond a certain limit.

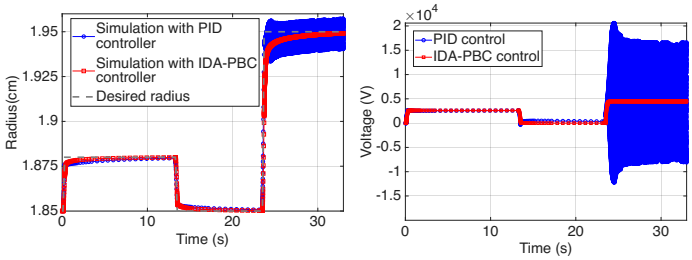

(a) Radius simulation. (b) Control voltage.

Fig. 13. Comparison between IDA-PBC controller and classical PID controller.

In order to analyze the robustness of the proposed controller against parameter uncertainties, we have applied the same IDA-PBC controller as in Fig. 13 to the plant where several identified parameters in Table 1 have been varied by 10%. The numerical results in the following Fig.14 indicate that the closed-loop system is highly sensitive to the relative permittivity, whereas it is less sensitive to the remaining parameters.

Remark 7. In order to validate the aforementioned robustness against parameter uncertainties, the designed controller was implemented on a different DEA tube in Section 5 than the one used for identification in Section 3.

Remark 8. On the basis of the proposed controller as formulated in Eq.(26), one can add an integral action as proposed in (Hammoud et al., 2024) such that the controller could reject external input disturbances. Depending on whether disturbances enter through the same port as the control input, one can classify them as matched, and unmatched disturbances (Ferguson et al., 2017). However, the integral action in (Hammoud et al., 2024) is only valid

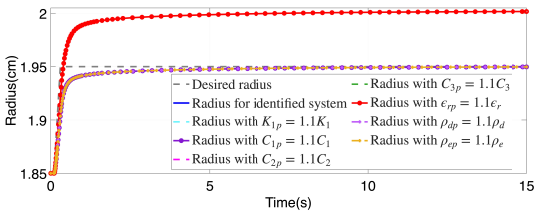

(a) Radius simulation.

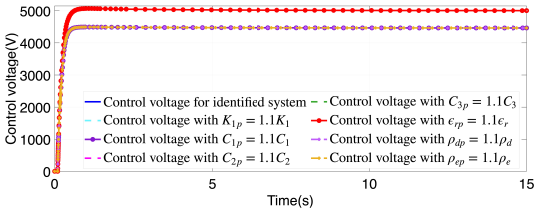

(b) Control voltage.

Fig. 14. Numerical robustness analysis w.r.t. parameter uncertainties, where K_{1p}, C_{1p}, C_{2p}, C_{3p}, ϵ_{rp}, ρ_{dp} and ρ_{ep} correspond to the values in the plant system, that are different from the identified values used in the IDA-PBC controller.

for matched disturbances, *i.e.*, voltage disturbances in this case. The rejection of unmatched disturbances (*e.g.* input pressure) necessitates further investigation.

5. CONTROL IMPLEMENTATION

In this section, the proposed controller is experimentally tested on the DEA platform as illustrated in Fig. 4. The DEA tube under investigation in this Section follows the same fabrication procedure as the one used for identification in Section 3, which allows us to analyze the robustness of the controller w.r.t. parameter uncertainties. The tube has an undeformed radius of 1.45cm, and is slightly prestretched by air pressure to achieve a deformed radius of 1.626cm. In order to avoid the deterioration of the DEA tube, the prestretch deformation in experiment is slightly smaller than in simulations as presented in Section 4.

Following simulations in Fig. 13 about comparisons between the proposed IDA-PBC controller and a classical PID controller, we have firstly implemented a PID controller on the DEA tube. The measurements of radius and control voltage are depicted in Fig.15. The desired deformation is shown by the black dashed line in Fig. 15a, corresponding to a rise time of 1s. As shown in Fig. 15, The PID controller is tuned to stabilize the DEA tube at the desired deformations of 0.03 mm and 0.05 mm. However, once the desired deformation increases to 0.1mm, the generated voltage appears to have very high frequency oscillations. It was necessary to reset the applied voltage to zero in order to avoid dielectric breakdown of the DEA. Compared with simulation results in Fig. 13, the PID control behaves even worse in real implementation.

In what follows, the proposed IDA-PBC controller is implemented. The closed-loop block diagram is presented in Fig.16. The control law (26) is a state feedback. A Luenberger observer is implemented in order to estimate the momentum and the electric charge with the measurement of the radial deformation.

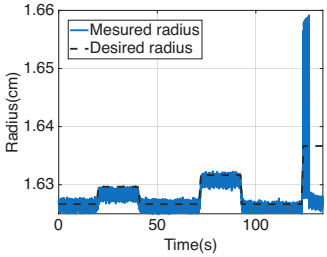

(a) DEA Radius measurement.

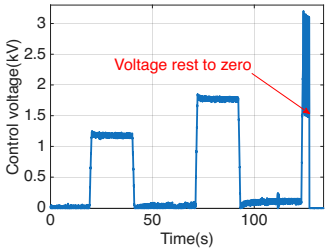

(b) Control voltage.

Fig. 15. Experiment results for a PID controller.

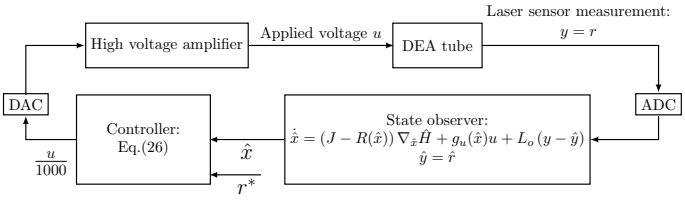

Fig. 16. Block diagram of the closed-loop, including the DEA tube, the developed control strategy and the implemented state observer, where L_o denotes the observer gain.

The simulation and measurement results of the proposed IDA-PBC controller are illustrated in Fig. 17. The desired deformations in Fig. 17a exhibit dynamics similar to those of the PID control shown in Fig. 15a, but with larger deformation levels of 0.2mm, 0.3mm, 0.4mm, and 0.5mm. The proposed IDA-PBC behaves better than the PID controller, and stabilizes the DEA at larger deformations, without generating oscillatory control voltage. As shown in Fig. 17b, the measured control input closely matches the simulation results. However, a static error can still be observed in Fig. 17a. This is mainly due to the chosen linear Luenberger observer. Therefore, a more advanced nonlinear observer dedicated to control of nonlinear systems necessitates further investigations.

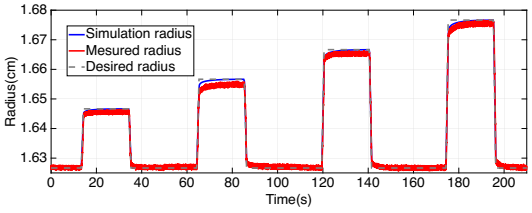

(a) DEA Radius measurement.

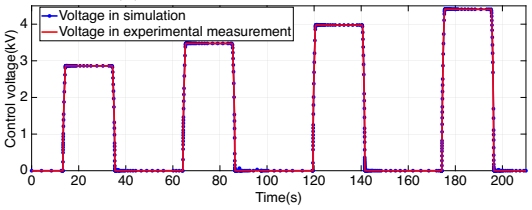

(b) Control voltage.

Fig. 17. Experiment validation of the control law.

6. DISCUSSION AND CONCLUSION

This paper presents a precise multiphysics dynamic model and a stabilization control strategy for a DEA tube. The

proposed model, developed using the port-Hamiltonian framework, addresses the key challenges associated with nonlinear material behavior, viscoelastic damping, and electromechanical coupling. Model parameters are identified using various input signal types and validated through five additional experimental scenarios. The model demonstrates high accuracy and robustness for deformation strains of up to 40 %.

Another contribution of this work is the design of an IDA-PBC controller that introduces a coupling term between the mechanical momentum and the electrical subsystem, modifies the closed-loop Hamiltonian, and increases dissipation within the electrical subsystem. The influence of control parameters on system performance and the generated control voltage has been thoroughly investigated. The controller was subsequently validated experimentally in a closed-loop configuration, demonstrating very high accuracy.

Future work will focus on integrating a robust controller to reject unmatched external disturbances in the closed-loop system, and on gaining further insight into nonlinear observer-based control.

ACKNOWLEDGEMENTS

We thank Armando Walter for the fabrication of DEA tubes and Amine Benouhiba for insightful discussions on the DEA characteristics.

REFERENCES

Acosta, J. and Astolfi, A. (2009). On the pdes arising in ida-pbc. In *Proceedings of the 48h IEEE Conference on Decision and Control (CDC) held jointly with 2009 28th Chinese Control Conference*, 2132–2137. IEEE. doi: 10.1109/CDC.2009.5400580.

Almanza, M., Clavica, F., Chavanne, J., Moser, D., Obrist, D., Carrel, T., Civet, Y., and Perriard, Y. (2021). Feasibility of a dielectric elastomer augmented aorta. *Advanced Science*, 8. doi:10.1002/advs.202001974.

Bernat, J., Koota, J., and Rosset, S. (2020). Identification of a nonlinear dielectric elastomer actuator based on the harmonic balance method. *IEEE/ASME Transactions on Mechatronics*, 14, 1–1. doi:10.1109/TMECH.2020.3044492.

Borja, P., Cisneros, R., and Ortega, R. (2016). A constructive procedure for energy shaping of port—hamiltonian systems. *Automatica*, 72, 230–234. doi:10.1016/j.automatica.2016.05.028.

Cisneros, N., Wu, Y., Rabenorosoa, K., and Gorrec, Y.L. (2025). Dynamic modeling of a curling hasel actuator using the port hamiltonian framework with experimental validation. *Mechatronics*, 109, 103342. doi: 10.1016/j.mechatronics.2025.103342.

Davies, J., Thai, M.T., Sharma, B., Hoang, T.T., Nguyen, C.C., Phan, P.T., Vuong, T.N.A.M., Ji, A., Zhu, K., Nicotra, E., Toh, Y.C., Stevens, M., Hayward, C., Phan, H.P., Lovell, N.H., and Do, T.N. (2024). Soft robotic artificial left ventricle simulator capable of reproducing myocardial biomechanics. *Science Robotics*, 9. doi: 10.1126/scirobotics.ado4553.

Duindam, V., Macchelli, A., Stramigioli, S., and Bruyninckx, H. (2009). *Modeling and Control of Complex Physical Systems*. Springer Berlin Heidelberg. doi: 10.1007/978-3-642-03196-0.

Ferguson, J., Donaire, A., and Middleton, R.H. (2017). Integral control of port-hamiltonian systems: Nonpassive outputs without coordinate transformation. *IEEE Transactions on Automatic Control*, 62, 5947–5953. doi: 10.1109/TAC.2017.2700995.

Hammoud, A., Liu, N., Le Gorrec, Y., Civet, Y., and Perriard, Y. (2024). Energy-based modeling and robust position control of a dielectric elastomer cardiac assist device. *IFAC-PapersOnLine*, 58(6), 25–30. doi: https://doi.org/10.1016/j.ifacol.2024.08.251. 8th IFAC Workshop on Lagrangian and Hamiltonian Methods for Nonlinear Control LHMNC 2024.

Harandi, M.R.J. and Taghirad, H.D. (2022). Solution of matching equations of ida-pbc by pfaffian differential equations. *International Journal of Control*, 95, 3368–3378. doi:10.1080/00207179.2021.1972345.

Javanmardi, N., Borja, P., Yazdanpanah, M.J., and Scherpen, J.M. (2025). Energy-based control approaches for weakly coupled electromechanical systems. *Automatica*, 177, 112336. doi:10.1016/j.automatica.2025.112336.

Kaaya, T., Wang, S., Cescon, M., and Chen, Z. (2022). Physics-lumped parameter based control oriented model of dielectric tubular actuator. *International Journal of Intelligent Robotics and Applications*, 6, 397–413. doi: 10.1007/s41315-021-00211-1.

Liu, N., Martinez, T., Walter, A., Civet, Y., and Perriard, Y. (2022). Control-oriented modeling and analysis of tubular dielectric elastomer actuators dedicated to cardiac assist devices. *IEEE Robotics and Automation Letters*, 7, 4361–4367. doi:10.1109/LRA.2022.3148981.

Liu, N., Wu, Y., and Gorrec, Y.L. (2021). Energy-based modeling of ionic polymer–metal composite actuators dedicated to the control of flexible structures. *IEEE/ASME Transactions on Mechatronics*, 26, 3139–3150. doi:10.1109/TMECH.2021.3053609.

Macchelli, A., van der Schaft, A., and Melchiorri, C. (2004). Multi-variable port hamiltonian model of piezoelectric material. In *2004 IEEE/RSJ International Conference on Intelligent Robots and Systems (IROS) (IEEE Cat. No.04CH37566)*, volume 1, 897–902 vol.1. doi:10.1109/IROS.2004.1389466.

Martinez, T., Chavanne, J., Walter, A., Civet, Y., and Perriard, Y. (2021). Design and modelling of a tubular dielectric elastomer actuator with constrained radial displacement as a cardiac assist device. *Smart Materials and Structures*. doi:10.1088/1361-665X/ac1fa8.

Martinez, T., Jahren, S.E., Walter, A., Chavanne, J., Clavica, F., Ferrari, L., Heinisch, P.P., Casoni, D., Haeberlin, A., Luedi, M.M., Obrist, D., Carrel, T., Civet, Y., and Perriard, Y. (2023). A novel soft cardiac assist device based on a dielectric elastomer augmented aorta: An in vivo study. *Bioengineering & Translational Medicine*, 8. doi:10.1002/btm2.10396.

Martins, F.G. (2005). Tuning pid controllers using the itae criterion. *International Journal of Engineering Education*, 21(5), 867.

Maschke, B., Schaft, A.V.D., and Breedveld, P. (1992). An intrinsic hamiltonian formulation of network dynamics: non-standard poisson structures and gyrators. *Journal of the Franklin Institute*, 329, 923–966. doi: 10.1016/S0016-0032(92)90049-M.

Ortega, R., der Schaft, A.J.V., Mareels, I., and Maschke, B. (2001). Putting energy back in control. *IEEE Control Systems*, 21, 18–33. doi:10.1109/37.915398.

Rizzello, G., Naso, D., and Seelecke, S. (2017). A thermodynamically consistent port-hamiltonian model for dielectric elastomer membrane actuators and generators. *IFAC-PapersOnLine*, 50, 4855–4862. doi: 10.1016/j.ifacol.2017.08.974.

Rizzello, G., Naso, D., Turchiano, B., and Seelecke, S. (2016). Robust position control of dielectric elastomer actuators based on lmi optimization. *IEEE Transactions on Control Systems Technology*, 24, 1909–1921. doi: 10.1109/TCST.2016.2519839.

Rizzello, G., Naso, D., York, A., and Seelecke, S. (2015). Modeling, identification, and control of a dielectric electro-active polymer positioning system. *IEEE Transactions on Control Systems Technology*, 23, 632–643. doi:10.1109/TCST.2014.2338356.

Rodríguez, H. and Ortega, R. (2003). Stabilization of electromechanical systems via interconnection and damping assignment. *International Journal of Robust and Nonlinear Control*, 13, 1095–1111. doi:10.1002/rnc.804.

Sarban, R. and Jones, R.W. (2012). Physical model-based active vibration control using a dielectric elastomer actuator. *Journal of Intelligent Material Systems and Structures*, 23, 473–483. doi: 10.1177/1045389X11435430.

Sen, A., Larson, J.S., Kashani, K.B., Libricz, S.L., Patel, B.M., Guru, P.K., Alwardt, C.M., Pajaro, O., and Farmer, J.C. (2016). Mechanical circulatory assist devices: a primer for critical care and emergency physicians. *Critical Care*, 20, 153. doi:10.1186/s13054-016-1328-z.

van der Schaft, A. (2017). *L2-Gain and Passivity Techniques in Nonlinear Control*. Springer International Publishing, 3 edition. doi:10.1007/978-3-319-49992-5.

van Kessel, R., Bauer, P., and Ferreira, J.A. (2021). Electrical modeling of cylindrical dielectric elastomer transducers. *Smart Materials and Structures*, 30, 035021. doi: 10.1088/1361-665X/abde4f.

Yeoh, O.H. (1993). Some forms of the strain energy function for rubber. *Rubber Chemistry and technology*, 66(5), 754–771.

Zhao, X., Hong, W., and Suo, Z. (2007). Electromechanical hysteresis and coexistent states in dielectric elastomers. *Physical Review B*, 76, 134113. doi: 10.1103/PhysRevB.76.134113.

Zou, J., Kassim, S.O., Ren, J., Vaziri, V., Aphale, S.S., and Gu, G. (2024). A generalized motion control framework of dielectric elastomer actuators: Dynamic modeling, sliding-mode control and experimental evaluation. *IEEE Transactions on Robotics*, 40, 919–935. doi:10.1109/TRO.2023.3338973.